Filtering of Milankovitch Cycles by the Thermohaline Circulation

DAVID BRICKMAN

Department of Fisheries and Oceans, Bedford Institute of Oceanography, Dartmouth, Nova Scotia, Canada

WILLIAM HYDE

Department of Oceanography, Texas A&M University, College Station, Texas

D. G. WRIGHT

Department of Fisheries and Oceans, Bedford Institute of Oceanography, Dartmouth, Nova Scotia, Canada

(Manuscript received 26 August 1997, in final form 7 July 1988)

ABSTRACT

A low-order, basin-averaged, coupled atmosphere–ocean paleoclimate model is developed and the results from a 3.2-Myr model paleointegration described. A three-basin version of the Wright–Stocker ocean model is used to compute the thermohaline circulation component of the climate system, with a six-basin energy balance atmosphere coupled to the ocean and land surfaces.

As expected, amplitude spectra of the paleo-integration results show that the annually averaged global air temperature (T_{atm}) closely follows the net radiation (Q_N), with power in the obliquity (40 kyr) and eccentricity bands (100 kyr and 400 kyr). However, there are also some unexpected results: the globally and annually averaged ocean temperature (T_{ocean}) is negatively correlated with T_{atm} in the obliquity band, T_{ocean} shows significant energy in the precessional band (20 kyr), and the response of T_{ocean} to Q_N variations is suppressed in the eccentricity band.

Physical explanations for the above results are presented and supported by a simple box climate model. This model helps to isolate and clarify the mechanism by which the ocean temperature varies significantly at precessional periods while the atmospheric temperature does not. The same model also illustrates the cause of the 40 kyr atmosphere–ocean temperature anticorrelation. Model integrations and analysis confirm that convection serves to rectify the zero annual-mean precessional forcing, resulting in 20 kyr energy in the ocean, which shows up only weakly in the atmosphere. The 40 kyr anticorrelation is the result of the latitudinal distribution of net radiation at obliquity periods, and thus can be reproduced only by a climate model with horizontal resolution. Ocean convection plays a critical role in determining both the 20 kyr and 40 kyr responses.

The suppressed response of the ocean in the eccentricity band is attributed to a combination of two effects. First, the larger albedo at high latitudes results in reduced variation of the air–sea heat flux at high latitudes so that variations in convection, and hence in deep water temperatures, are also reduced. Second, the nonlinearity of the equation of state for seawater contributes latitudinal variations in ocean densities, which result in changes in the overturning circulation, which further suppress the ocean temperature variations in the eccentricity band.

The implications of the authors' results for interpretations of the paleoclimate record are discussed.

1. Introduction

The basic forcing for the climate system is the radiation received at the top of the atmosphere. The large-scale and low-frequency variations of insolation are determined by the orbital parameters obliquity, eccentricity, and the longitude of perihelion (precession), and there is ample evidence (Imbrie 1984; Herbert and Fischer 1986; Olsen 1986; Pisias et al. 1995) that the earth's climate experiences changes at these ''Milankovitch'' frequencies.

The question of how orbital change is translated to the paleoclimatic record has been studied for several decades (Hays et al. 1976; Saltzman and Sutera 1984; Hyde and Peltier 1987; Short et al. 1991). Explanations exist for some of the power seen in the paleoclimate record but there are still numerous areas of uncertainty. For example, the strong 100 kyr signal observed in the climate record over the past 900 kyr has been attributed to the interaction of ice sheets and seasonality (Hyde and Peltier 1987; Tarasoff and Peltier 1997). Precession plays a critical role in these interpretations. Since precession redistributes insolation through the year without

Corresponding author address: Dr. David Brickman, Department of Fisheries and Oceans, Bedford Institute of Oceanography, Dartmouth, NS B2Y 4A2, Canada.
E-mail: dbrick@diligent.bio.dfo.ca

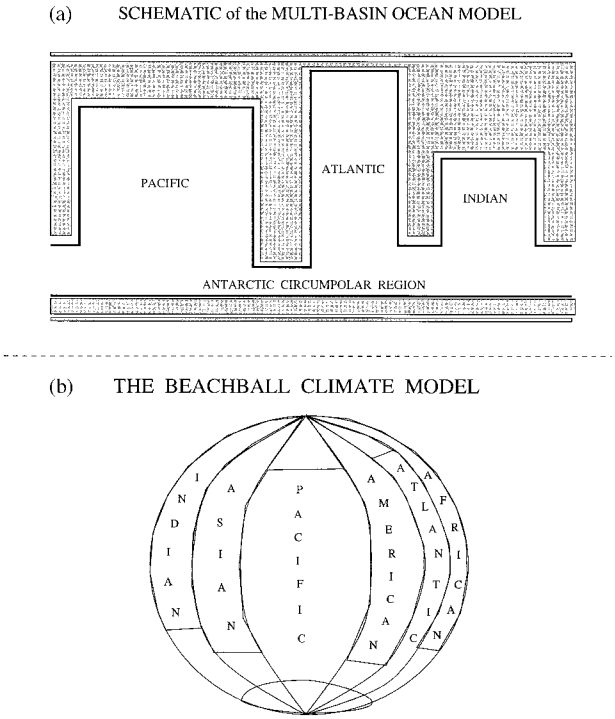

FIG. 1. Schematic of the climate system showing (a) the basins of the ocean model and (b) the beachball analogy.

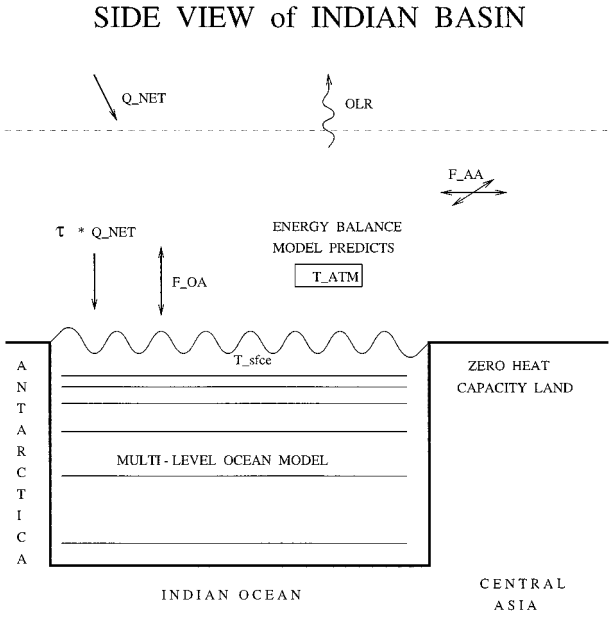

FIG. 2. Side view of the Indian basin showing more details of the coupled system. Here, Q_{NET} and OLR are the net incoming shortwave and outgoing longwave radiations at the top of the atmosphere, τ is the fraction of Q_{NET} that reaches the ocean surface and is absorbed there, F_{OA} is the net heat exchange across the air–sea interface, and T_{sfce} and T_{ATM} are the surface ocean and atmosphere temperatures, respectively. Atmospheric fluxes, F_{AA}, are in the N–S and E–W directions.

affecting the annual average, a rectification mechanism is clearly required to produce nonzero annual average forcing from this purely seasonal input. The studies mentioned above demonstrate that ice-sheet variations can provide such a mechanism. However, deep sea cores show evidence of precessional power even at times when there was little or no land ice (Pisias et al. 1995), so it appears that there are other rectification mechanisms in the climate system. One purpose of the present work is to investigate the possibility that the thermohaline circulation of the global ocean may act as a rectification mechanism to generate low-frequency signals from variations in the amplitude of seasonal forcing.

Zonally averaged ''2½''-dimensional thermohaline models coupled to simple energy balance models (EBMs) of the atmosphere have had considerable success both in reproducing the current state of the ocean and in providing plausible mechanisms for various paleoclimatic events such as the Younger Dryas (Wright and Stocker 1991) and Dansgaard–Oeschger oscillations (Sakai and Peltier 1995). A weakness of such models, however, lies in their zonally averaged representation of the atmosphere, which does not resolve the land–sea contrast in surface temperature (Hyde et al. 1989). This contrast is potentially important for at least two reasons. First, a larger signal in air temperature is expected over land than over the oceans so a zonally averaged EBM will underestimate the observed terrestrial signal. Second, it seems plausible that zonal variations in surface air temperature may affect the stability of the thermohaline circulation. For example, a decrease in the strength of the overturning circulation in the Atlantic basin will be accompanied by a decrease in the surface temperature at high northern latitudes, and this will tend to reinforce (hence stabilize) the overturning within this basin. Since zonal averaging will reduce the magnitude of the atmospheric temperature variations by artificially spreading them around the globe, it is possible that such averaging affects the stability of the thermohaline circulation.

In this paper we describe a coupled atmosphere–ocean climate model containing longitudinal resolution in both the ocean and atmosphere, and examine the results from a 3.2 Myr model ''paleo-integration.'' The coupled model divides the earth into six north–south atmospheric stripes, and three ocean basins coupled through a circumpolar southern ocean. The evolution of both temperature and salinity, averaged over the width of each basin, is modeled, but only temperature results are discussed here. Effectively, the model describes the climate on a ''beachball'' earth, where each stripe contains an atmosphere overlying ocean or land depending on latitudinal position. The Wright–Stocker ocean model was used to compute the ocean's thermohaline circulation, and a six-basin energy balance model is developed to represent the atmosphere. The resulting idealized climate system is illustrated in Figs. 1 and 2.

At the top boundary of the model the atmosphere

receives net solar radiation Q_N and emits longwave radiation OLR as a function of its temperature [i.e., OLR $= f(T)$]. Here Q_N is a function of the planetary albedo and the incoming solar radiation. In this paper we take the albedo to be fixed at the current annually averaged climatology. Therefore, Q_N depends solely on the orbital parameters of the earth so that we will consider *only* the effects of changes in incoming radiation on the coupled system. As well, we run the model in ice-free mode in order to isolate the effects of ocean circulation and convection on the climate system. Clearly, this model is only one of a possible heirarchy of coupled models, but the results presented here should represent a useful benchmark for comparison with the results from future studies.

The outline of this paper is as follows. Section 2 describes the atmosphere–ocean model in more detail. The next section discusses the setup of the paleo-integration and issues relevant to it. Section 4 reports model results and highlights questions arising from the paleo-integration. These questions are answered in sections 5 and 6 with the aid of an even simpler atmosphere–ocean box model. A summary and conclusions are presented in the last section.

2. The atmosphere–ocean climate model

In this section we discuss the coupled model geometry, the atmosphere and ocean model components, the coupling procedure, and the comparison between the model estimate of the current climate and the actual current climate.

a. Model geometry

As mentioned above the atmosphere–ocean model consists of six longitudinal bands in the atmosphere coupled to three zonally averaged ocean basins and the intervening land surfaces. The three ocean basins (representing the Pacific, Atlantic, and Indian Oceans) are connected in the south by a circumpolar Southern Ocean (Stocker et al. 1992; Fig. 1a). (The Southern Ocean is actually represented by six regions for ease of coupling with the atmosphere, but instantaneous zonal mixing between these regions eliminates the dynamical distinction between them.) The six longitudinal bands of the atmosphere represent the longitude bands overlying the three ocean regions mentioned above, plus the bands overlying the Americas, Europe–Africa, and Asia–Australia. The ocean basins and atmospheric regions are each assigned a constant longitudinal width, roughly equal to the average width of the equivalent real-world feature (Fig. 1). The zero heat capacity land has no thermodynamic effect on climate while the oceanic regions allow for air–sea heat exchange as will be described below. As in Stocker et al. (1992b) the ocean basins are of constant depth, while the atmospheric regions are vertically averaged as in North (1975) (Fig. 2).

b. The atmospheric model

The ocean model is essentially unchanged from that discussed in previous publications (Wright and Stocker 1991; Stocker et al. 1992b) and details will not be repeated here. The inclusion of zonal resolution in the atmospheric EBM is new and hence our discussion focuses on this feature and the ocean–atmosphere coupling.

The atmospheric model describes the evolution of the surface temperature (T_{ij}) as a function of latitude (j) for each of the zonally averaged basins (i). Interbasin exchange is a function only of the temperature difference between basins. The model allows for both diffusive and advective fluxes in the horizontal, but the version used here was purely diffusive. Air–sea exchange is determined precisely as in Stocker et al. (1992b). The governing equation for basin i at latitude j is

$$\frac{\partial T_{ij}}{\partial t} = \frac{1}{R^2 \cos\phi}\frac{\partial}{\partial \phi}\left(\cos\phi \kappa_{\text{ns}} \frac{\partial T_{ij}}{\partial \phi}\right) + \frac{1}{R^2 \cos^2\phi}\frac{\partial}{\partial \lambda}\left(\kappa_{\text{ew}} \frac{\partial T_{ij}}{\partial \lambda}\right) + \frac{1}{\rho C_P H}[(Q_N - \text{OLR}) - F^{ij}_{\text{OA}}], \quad (1)$$

where Q_N is the net solar radiation, OLR is the outgoing longwave radiation, F_{OA} is the flux from ocean to atmosphere, κ is the diffusivity in the north–south (ns) or east–west (ew) direction, R is the earth's radius, ρ is density, C_P is specific heat, H is the scale height of the atmosphere, ϕ is latitude, and λ is longitude. In the model run considered here, we take

$$Q_N = [1 - \alpha(\phi)]Q(\phi, t), \quad (2)$$

where $Q(\phi, t)$ is the shortwave radiation at the top of the atmosphere and α is the planetary albedo. The outgoing longwave radiation is given by

$$\text{OLR} = A(\phi) + BT_{ij}, \quad (3)$$

where B is a constant set equal to 2 W m^{-2} °C^{-1}. We calculate $\alpha(\phi)$ using satellite data for Q_N, and $A(\phi)$ is estimated using data for OLR and the zonally and annually averaged temperature. (Here A and α were taken to be functions of latitude only due to data availability at the time the model was first run.) Note that the atmospheric model just described has tunable parameters: the horizontal diffusion terms (viz., κ_{ns} and κ_{ew}), and coefficients in the air–sea coupling term F_{OA}. These are determined as discussed below.

c. Atmosphere–ocean coupling

Our goal is to couple the atmosphere to the ocean in a way that produces a stable climate that resembles the current climate in its major characteristics (e.g., zonally averaged ocean circulation and atmospheric temperature fields). To do so, we use the technique developed by Stocker et al. (1992), adapted to account for the multibasin atmospheric model. In this method, the ocean is

first spun up to equilibrium with the surface temperature and salinity fields restored to the present-day annually and basin-averaged values of Levitus (1993) on a timescale of 50 days. At the end of this spinup period, the ocean surface fluxes of heat and moisture (represented in our rigid-lid model as a virtual salt flux) are diagnosed and used as the bottom boundary conditions for the atmospheric model.

The coupling proceeds in three stages. First, a zonal and annual average of (1) is performed, which yields

$$0 = \frac{1}{R^2 \cos\phi}\frac{\partial}{\partial\phi}\left(\cos\phi\kappa_{\rm ns}\frac{\partial T_j}{\partial\phi}\right) + \frac{1}{\rho C_P H}\{[Q_N - (A + BT_j)] - F^j_{\rm OA}\}, \quad (4)$$

where quantities with a subscript j represent zonal averages around the entire globe. Note that the simple form of this equation depends on the linearization of the OLR term.

The values of $F^j_{\rm OA}$ are determined by the surface fluxes across the ocean surface at the end of the initial ocean-only spinup period and Q_N, T_j, A, and B are estimated from observations. Thus, (4) can be trivially solved for $\kappa_{\rm ns}(\phi)$. Next, we want to determine values of $\kappa_{\rm ew}$ to be consistent with the climatological, annually averaged temperatures T_{ij}. This was done using an optimization routine that forward integrates (1) to equilibrium finding the $\kappa_{\rm ew}$ that minimizes the ''squared error'' between the T_{ij} data and the final equilibrium temperatures. The ''squared error'' includes a contribution that penalizes nonphysical diffusivities. Note that $\kappa_{\rm ew}$ (as well as $\kappa_{\rm ns}$) could, in principle, be a function of ϕ, λ, T, etc., but for this study we have chosen to consider only $\kappa_{\rm ew}$ = const and $\kappa_{\rm ew} = \kappa_{\rm ew}(\phi)$.

Finally, with the atmosphere and ocean coupled and adjusted to a steady state, the ocean surface flux, previously derived from an ocean-only spin up, can be converted to a true interactive coupled ocean–atmosphere flux of the form $F_{\rm OA}$ = net solar flux + net infrared flux + sensible heat flux + latent heat flux. That is [following Stocker et al. 1992, their Eq. (17)], for the ijth basin,

$$F_{\rm OA} = -(1 - a)Q_N + (\sigma\epsilon_m T_m^4 - \sigma\epsilon_a T_a^4) + D(T_m - T_a) + E, \quad (5)$$

where a is the atmospheric absorptivity, ϵ represents emissivity, D the sensible heat flux exchange coefficient, $E = c_e f(T_m, T_a)$ the evaporation [f is specified as in Stocker et al. (1992)], and the subscripts m and a stand for mixed layer and atmosphere, respectively. In principle, a, ϵ_o, ϵ_m, ϵ_a, D, and c_e could each be treated as free parameters to be determined by the optimization procedure. However, we have followed the more pragmatic method introduced by Stocker et al. (1992) in which a, ϵ_o, ϵ_m, D, and E are determined from climatological data, then c_e is determined to be consistent with the bulk formula for evaporation and ϵ_a is determined by (5).

The above procedure produces an atmosphere and ocean that are coupled and in steady state with respect to annually averaged quantities. This result is satisfactory for many coupled atmosphere–ocean problems. However, for our present purpose it is necessary that the seasonal cycle be included in the solar forcing. Unfortunately, an atmosphere and ocean that are in equilibrium with annually averaged forcing do not necessarily remain unchanged, even in their annually averaged properties, when a seasonal cycle is introduced. The problem of optimized coupling with seasonal variations included is currently being investigated. In the meantime, the parameter determination and coupling procedure discussed above was considered to be a reasonable starting point for integrations that include seasonally varying radiative forcing. After the model was coupled, the seasonal cycle in shortwave radiation was initiated and the model was run in fully interactive mode for a 5 kyr equilibration period. The model was thus adjusted to the current seasonally varying forcing before beginning the paleo experiment (i.e., before changing the orbital parameters to those corresponding to a different epoch).

d. Fit to current climate

The optimization routine tries to find the $\kappa_{\rm ew}$ that yield the smallest squared error between the air temperature data and equilibrium model temperature summed over the 21° lat × six-basin grid. (We ignore the contribution to the cost function from penalizing nonphysical diffusivities as this was, in general, negligible.) The evaluation of the coupling procedure can be done at two times: (phase 1) after the optimization routine, when the atmosphere and ocean are coupled to the annual average climate; or (phase 2) after the seasonal cycle has been turned on. For simplicity the choice for $\kappa_{\rm ew}$ was made after the first phase of the coupling procedure.

The model's temperature structure corresponding to the current radiative forcing was compared to the Crutcher and Meserve atmospheric dataset (Crutcher and Meserve 1970), as well as to data from the ''GEDEX'' CD-ROM. To make a quantitative comparison of the surface air temperatures, the constant width regions of the model must be identified with appropriate regions in the real world. For example, the average air temperature at 50°N over North America was taken as the average over the width of the continent at that latitude and applied to the narrower (40°) model representation of that basin. The full mapping used to make the desired comparisons is shown in Fig. 3.

The model with $\kappa_{\rm ew} = f(\phi)$ had an rms temperature error of 2.04°C and thus was marginally superior to the $\kappa_{\rm ew}$ = const model, which had an error of 2.15°C. In both cases longitudinal errors were as large as 7°C. If all $\kappa_{\rm ns}$ are physically acceptable (i.e., $\kappa_{\rm ns} > 0$) the cou-

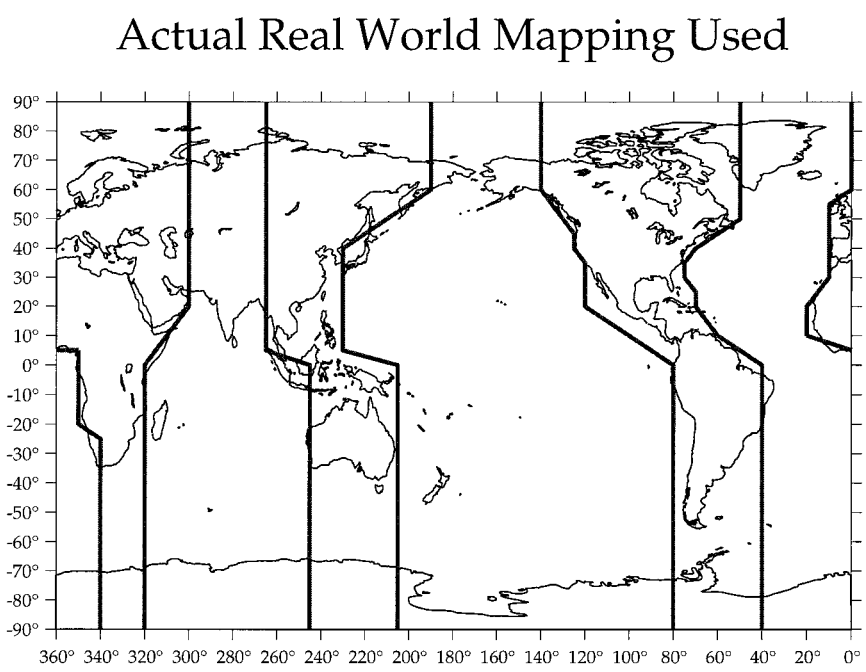

FIG. 3. The mapping used to determine observational estimates of the temperature variations in the six atmospheric longitude bands. This mapping illustrates the correspondence between the actual ocean–land basins and the constant longitudinal basins used in the model.

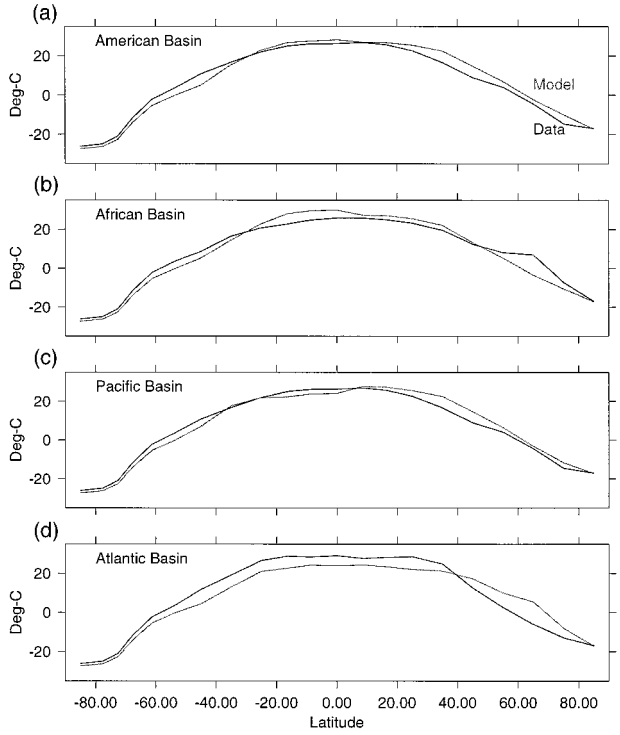

FIG. 4. The annual averages of the observed air temperatures and the corresponding model estimates after 5 kyr of integration with the seasonal cycle in shortwave radiation included.

pling method ensures a zonally averaged temperature error of zero [see (4)]. For the case where any $\kappa_{ns} < 0$ (which typically occur near the equator where the effects of the Hadley cell have been neglected), a default value of 10^6 m^2 s^{-1} was used. This resulted in negligible zonal temperature errors. Thus while temperature discrepancies could be large in a given basin, the method yields small or zero errors in zonally averaged temperatures and the globally averaged temperature.

Figures 4 and 5 show comparisons between annually averaged atmospheric and oceanic surface temperatures and data after the model was run for 5000 yr in coupled mode with the present-day seasonal cycle in shortwave radiation. During this time the rms temperature error increased from 2.04° to 2.74°C. From Fig. 4 it is clear that the model captures the essentials of the annually averaged air temperature above both land and ocean, although regions of differences ~7°C persist through the spinup period. While the fit is clearly not perfect, it is in or near the ensemble average of the GCMs studied by Yip and Crowley (1994), and is probably as good as can be expected from a coarse-resolution diffusive model. Figure 5 shows that the introduction of seasonal cycle forcing changes the ocean surface temperatures as well, but again we consider the discrepancies to be within an acceptable range.

The most substantial change observed as the coupled system adjusts to the initiation of seasonally varying forcing is in the global ocean temperature. Figure 6 shows the annually averaged global ocean and atmospheric temperatures, and the maximum Atlantic over-

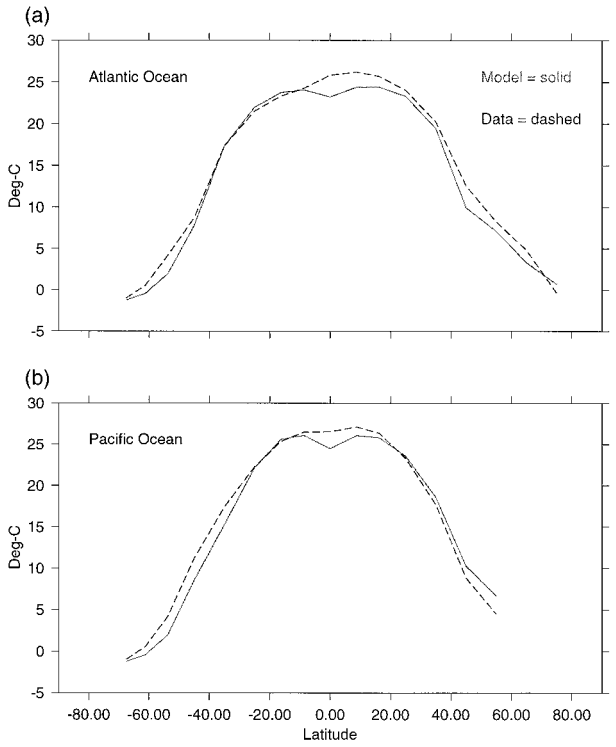

FIG. 5. The annual averages of the observed ocean surface temperatures and the corresponding model estimates after 5 kyr of model integration with the seasonal cycle in shortwave radiation included.

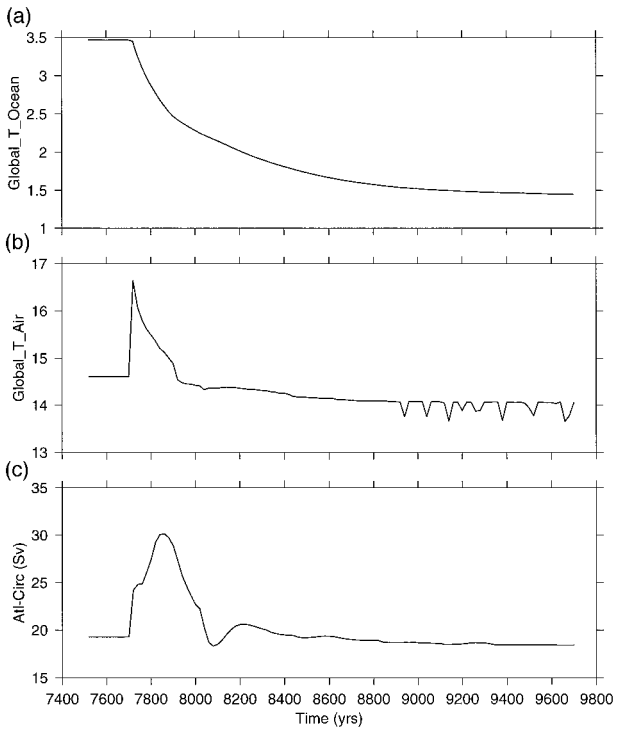

FIG. 6. Evolution of global ocean and atmosphere temperatures and the Atlantic circulation during the integration period after the present-day seasonal cycle is initiated.

turning streamfunction (Atl_circ), during the coupled spinup phase. When the seasonal cycle is turned on, both the atmospheric temperature and Atl_circ experience abrupt changes to higher values but return to values near the initial conditions over the next few hundred years. On the other hand, the globally averaged ocean temperature drops to about 1.5°C and remains there. This heat loss may be due to the calculation of coupling coefficients using annually averaged quantities (e.g., temperature) where the actual process may be poorly represented by annual means (e.g., exchanges in polar regions), or oversimplification of controlling feedback mechanisms. In any case, this discrepancy indicates an area where further work needs to be done.

In brief, we find that the basin-averaged atmospheric model with κ_{ns} and κ_{ew} functions of latitude coupled to the Wright–Stocker ocean model yields a stable climate reasonably similar to current day, and acceptable as a starting point for the present study.

3. The paleoclimate experiment

The model run used to investigate the response to long-term changes in orbital forcing was conducted as follows. First, the ocean and atmosphere components of the model were coupled and run to equilibrium under current climatology, including the current seasonal cycle in incoming shortwave radiation. After an equilibrium state under present-day conditions was achieved, the orbital parameters controlling solar radiation at the top of the atmosphere—eccentricity, obliquity, and ''precession''—were set to values corresponding to some time in the past and the integration was continued with the orbital forcing continually updated.

It was found that model results at time t were not sensitive to the start time, t_0, for the paleo-integrations provided $t - t_0$ was greater than a few thousand years. That is, the model lost memory of its initial conditions over a timescale of a few thousand years. This result clearly depends on the fact that the system did not undergo any major mode transitions. This is a useful result since it means that shorter runs (on either the same or different machines) can be ''stitched'' together into one long run. In practice, model runs were overlapped by 5 kyr and the initial 5 kyr of each run were discarded (after verifying agreement with the previous run at the end of this period). In this manner, a continuous time series extending over 3.2 Myr was generated. The model was integrated asynchronously, with an ocean time step of 20 days, and an atmospheric time step of 2 days. (An implicit numerical scheme was used in the atmospheric integration in order to allow the 2-day time step.) Data was stored typically every 200 yr, with occasional periods of 2- or 20-yr output.

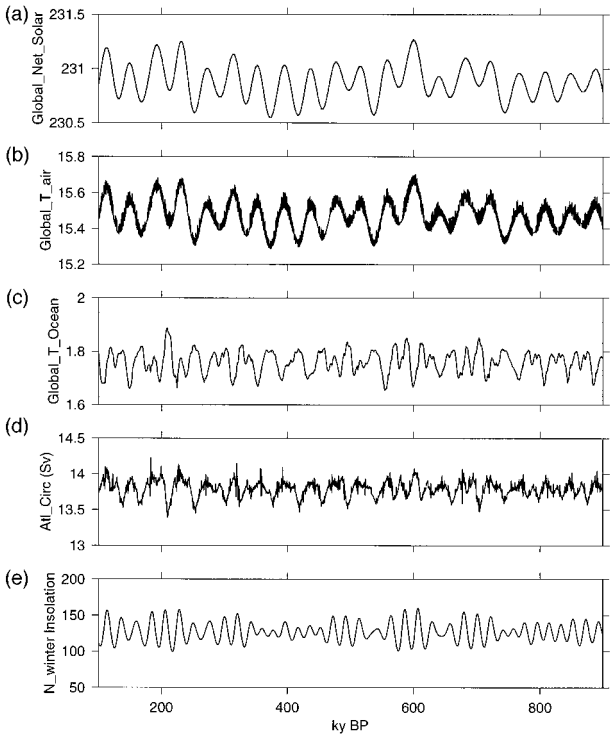

FIG. 7. The Q_N, T_{atm}, T_{ocean} Atl_circ, N-winter insolation: sample of model results without any filtering. Note that time is given in kyr *before* present.

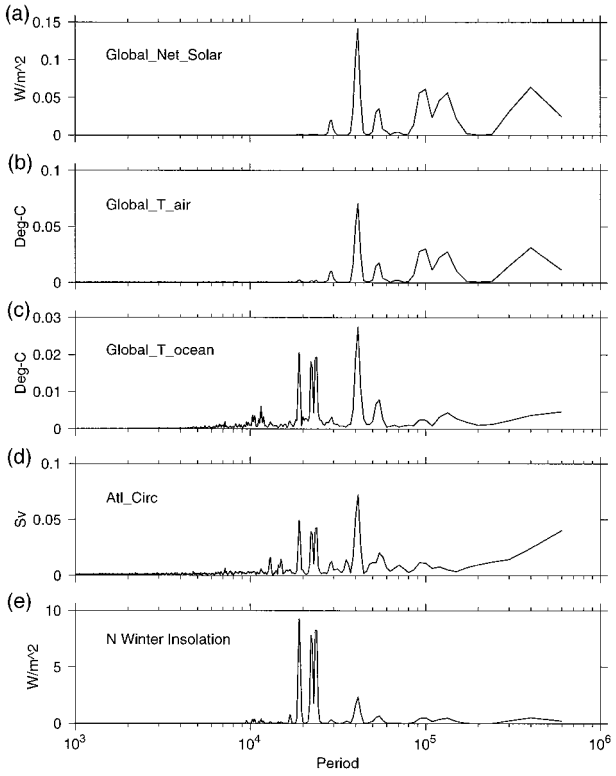

FIG. 8. Amplitude spectra of variables shown in Fig. 7.

a. Background on paleoclimate forcing

It is useful to review some basic properties of the radiative forcing due to orbital parameter changes in order to help interpret the results of our paleoexperiments.

The precession of the equinoxes changes the relative position of the vernal equinox (when days and nights are of equal length) with respect to perihelion (when the earth is nearest to the sun) in the earth's orbit, with a period of 22 kyr (relative to the fixed stars, precession has a longer period of 26 kyr, but the orbit of the earth itself changes, resulting in the shorter period of relevance to the present study). The dynamically important result of precession is to redistribute insolation throughout the year at the top of the atmosphere, *without affecting the annual average receipt at a given latitudinal band* (though seasonal changes in albedo may result in net radiation changes). Thus precessional changes make the seasonal cycle of radiation more or less extreme. For example, today's orbit places the earth at perihelion during Northern Hemisphere winter, which is thus ameliorated, as the earth receives about 3% more insolation at perihelion than average. Eleven thousand years ago, on the other hand, the earth was at aphelion during Northern Hemisphere winter, and winters were correspondingly more severe.

Changes in obliquity redistribute insolation at the top of the atmosphere among latitudes *without affecting the planetary average.* Higher obliquities result in more polar and less tropical insolation. At a given latitude, this can change both the annual average receipt of insolation and the strength of the seasonal cycle. Obliquity varies with a dominant period of 41 kyr. Note that if the planetary albedo is a function of latitude, as is the case in our model, then the global and annually averaged *net* absorbed radiation will have power at obliquity frequencies.

The dominant eccentricity variations are at periods near 100 and 400 kyr. Eccentricity variations have a twofold effect. First, eccentricity variations modulate the strength of the precessional effect (the 3% figure quoted above is about 2*e*, where *e* is the current eccentricity) so that the power spectrum of the precessional effect has a number of peaks in the region of 19–23 kyr. The secondary effect of eccentricity is to change the time-averaged earth–sun radius and thus the annual global radiation received (orbits with large eccentricity have smaller time-averaged earth–sun radii). This can lead to small changes in the globally averaged temperature.

4. Results from the paleoexperiment

Figure 7 shows a sample of relevant variables from the model run. Plotted are annual and global averages of the net solar radiation, air temperature, and ocean

temperature. The last two panels show the annual average maximum overturning streamfunction in the Atlantic basin (Atl_circ) and insolation at northern winter (band 45°–75° lat). The latter is a measure of the precessional contribution to the radiative forcing. Amplitude spectra for these quantities are plotted in Fig. 8.

The following points are of interest:

1) The global air temperature is almost a perfect mirror of Q_N, except that it has small amplitude higher-frequency variability superimposed on it. Closer inspection of the data show that this variability has a period of about 100 yr and is related to slight changes in ocean circulation and convection. The amplitude spectra show energy in the 40 kyr (obliquity), and the 100 kyr and 400 kyr (eccentricity) bands.
2) The global ocean temperature has significant energy in the 20 kyr (precessional) band, as well as the 40 kyr band. At 40 kyr we see from the raw data that the ocean and atmosphere temperatures are anticorrelated. We will show that this is due to the spatial distribution of the obliquity forcing plus oceanic convection.

   With respect to the power at 20 kyr, the globally averaged energy equation

$$\frac{d}{dt}[(\rho C_P V)_{oc} T_{ocean} + (\rho C_P V)_{atm} T_{atm}] = [Q_N - (A + BT_{atm})](4\pi R^2), \quad (6)$$

   where V is volume and the other symbols have their usual meaning, raises the question: How can T_{ocean} contain significant energy in the 20 kyr band while T_{atm} and Q_N do not? We will refer to these two somewhat counterintuitive results as ''the 20 kyr/40 kyr dilemma.''
3) The Atl_circ and T_{ocean} spectra are each similar to the northern winter (N-Wint) insolation in the 20 kyr band. Phase spectra show that T_{ocean} is 90° out of phase with the northern winter insolation, indicating that T_{ocean} acts as an integrator of the northern winter insolation.
4) The spectrum of T_{ocean} shows that the global ocean response in the eccentricity band is suppressed relative to the forcing Q_N. Phase spectra of T_{ocean} and Atl_circ (see later) show that T_{ocean} is approximately 180° out of phase with Atl_circ at periods less than 100 ky (i.e., low ocean temperatures occur coincident with stronger ocean circulation), but in phase in the eccentricity band.

In the next two sections we present physical explanations for each of these results aided by a highly simplified coupled atmosphere–ocean climate box model, which helps to illustrate and confirm these explanations. The 20 kyr/40 kyr dilemma is discussed first, followed by an explanation for why the global ocean's response differs from the atmosphere's at long periods.

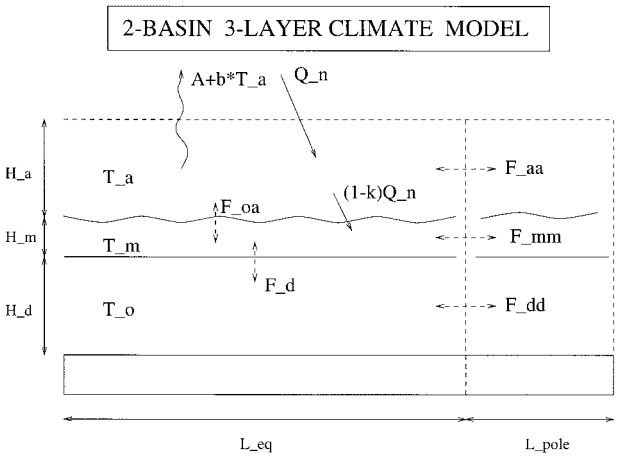

FIG. 9. Schematic illustration of the two-basin three-layer model.

5. The 20 kyr/40 kyr dilemma

a. The 20 kyr energy and ocean convection

The first question that we address is why the ocean response includes significant energy in the 20 kyr precession band, but the atmosphere does not. We hypothesize that this is due to the rectifying effect of convection in the ocean and then present results from a two-(north–south) basin three-layer climate model to support this idea. For brevity we relegate the details of this model to an appendix.

The most important point to be made is that convection serves as a mechanism to rectify seasonal cycle forcing such that amplitude modulation of the seasonal cycle results in deep ocean temperature variations at the modulation frequency, with very little effect on surface conditions. Figure 10 shows a schematic of the process. A seasonally low radiation input cools the mixed layer causing convection, which cools the deep ocean, moving a quantity of heat to the mixed layer–atmosphere. Due to the low thermal mass/fast adjustment timescale of the mixed layer–atmosphere this flux causes a rapid increase in temperature that is efficiently radiated to outer space. On the other hand, the deep ocean is effectively isolated from such rapid surface processes and the cooling effect accumulates over the years. Based on this idea, we expect that the changes in the deep ocean temperature, T_d, should be related to the precessional forcing, which controls the seasonality in polar radiation.

The general model, shown in Fig. 9, consists of equatorial and polar boxes, each with an atmosphere overlying an ocean mixed layer, and a deep ocean region. The fluxes between boxes are modeled as a transfer coefficient (q in W m^{-2} K^{-1}) times a temperature difference, resulting in an exchange time between boxes given by $\tau \equiv (\rho C_P \mathcal{L})/q$, where $\mathcal{L}$ is a relevant length scale (either horizontal or vertical). The only nonlinearity in the model is a convection scheme whereby the timescale of vertical exchange is greatly reduced when the density gradient is statically unstable. This nonlin-

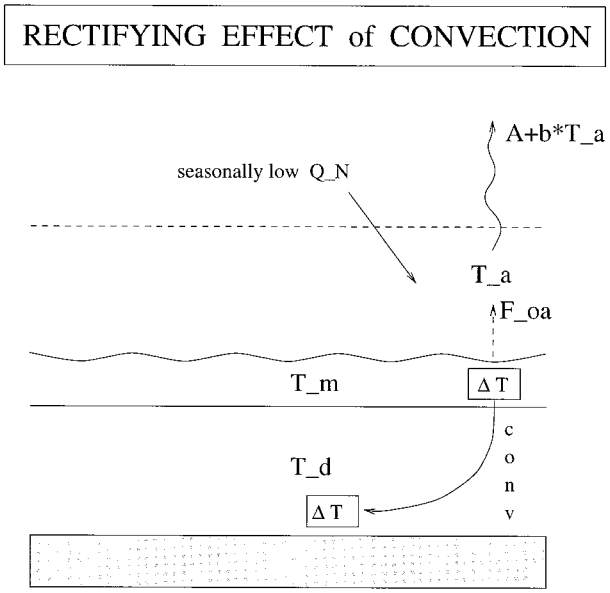

FIG. 10. Schematic illustration of the rectifying effect of convection.

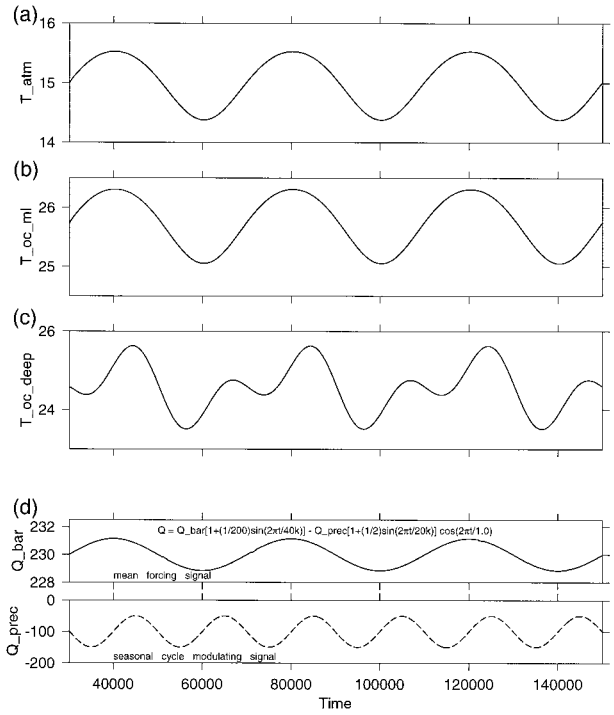

FIG. 11. Annually averaged variables from the global model.

earity serves as the mechanism for rectification of seasonal cycle forcing.

To illustrate the rectifying effect of convection, it suffices to consider an isolated vertical column. Thus, we consider the results of numerical experiments performed with a simplified version of Eqs. (A1)–(A3) (the ''global model'') in which the horizontal exchange terms are omitted. For these experiments, the paleonet radiative forcing was modeled to be similar to the paleoforcing for the beachball (WS) model, that is, as an annual-mean term that changes on a 40 kyr timescale and an amplitude-modulated seasonal cycle term representing a precessional 20 kyr effect with zero annual mean:

$$Q_N(t) = \overline{Q}[1 + (1/200)\sin(2\pi t/40k)] - Q_{\text{prec}}[1 + (1/2)\sin(2\pi t/20k)] \times \cos(2\pi t/1.0), \quad (7)$$

where $\overline{Q} = 230$ and $Q_{\text{prec}} = 100$.

With convection turned off it was found, as expected, that all temperatures followed the mean paleoforcing

$$\overline{Q}(t) = \overline{Q}[1 + (1/200)\sin(2\pi t/40k)].$$

Figure 11 shows the result with the convective scheme on. We see that T_d shows 20 kyr precessional power but $T_a \approx \overline{Q}(t)$ with no (apparent) 20 kyr power. While we now see how the global ocean temperature can have oscillations in the precessional band, we seem, in light of the global energy Eq. (6), to again encounter the 20 ky dilemma.

Figure 12 is a plot of Q_N and OLR, (Q_N − OLR), and the convective flux from the global model. The top panel shows that ($A + BT_a$) is not a perfect 40 kyr sinusoid, the difference showing up as the 20 kyr signal seen in Fig. 12b. This 20 kyr signal is a reflection of the annually averaged convective flux—the rectification process—shown in Fig. 12c. The rapid adjustment of the mixed layer–atmosphere limits the magnitude of this

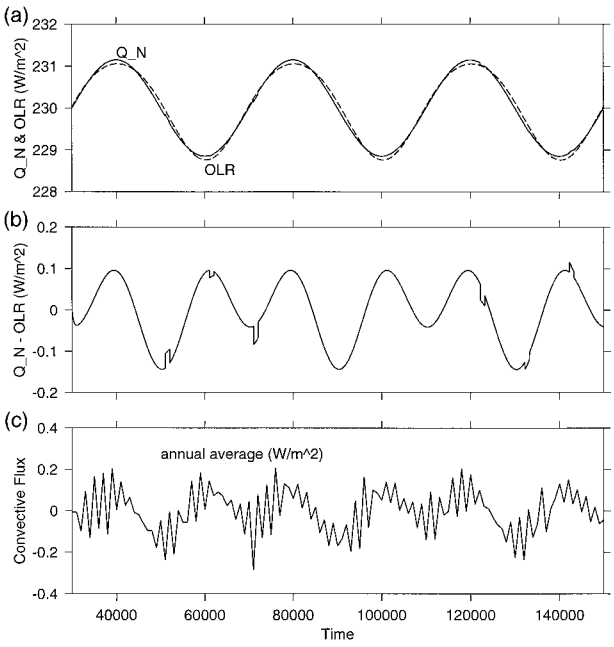

FIG. 12. (a) The Q_N and OLR, (b) Q_N − OLR, and (c) the globally averaged vertical heat flux associated with convective mixing in the model ocean.

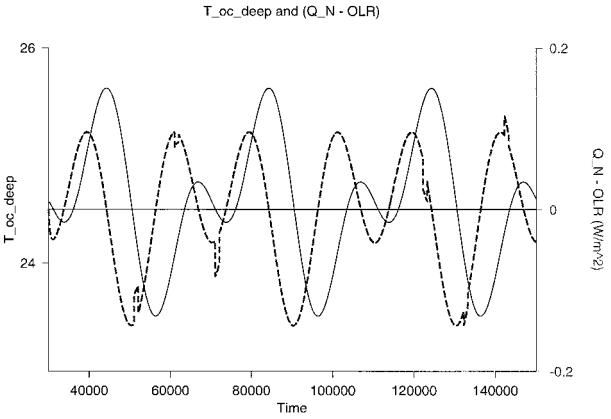

FIG. 13. The T_d (solid line) and Q_N − OLR (dashed line) illustrating the integrating nature of T_d. For periods when Q_N − OLR is negative, T_d declines, and vice versa.

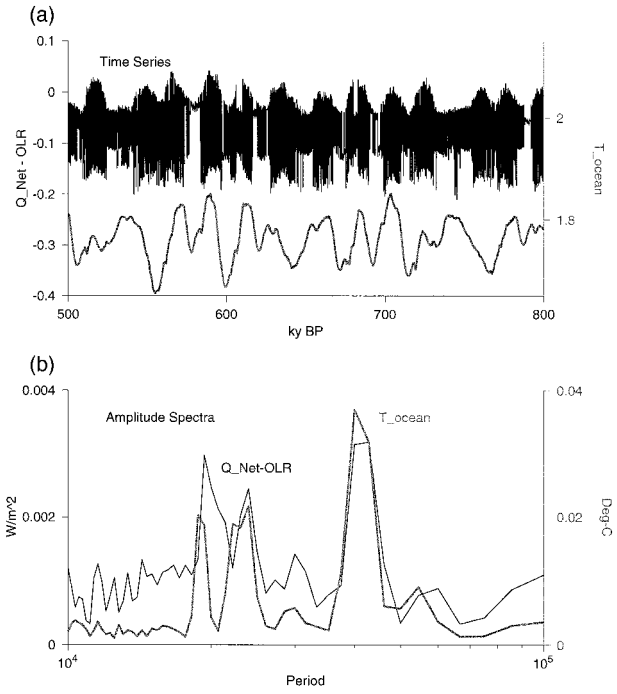

FIG. 14. (a) Global ocean temperature and (Q_N − OLR) from the WS climate model. (b) Amplitude spectra of the results shown in (a).

effect, which means that the term (Q_N − OLR), the source of the 20 kyr power in T_a, is doomed to be the small residual of two large numbers.

Figure 13 shows that the deep ocean temperature looks like an ''integrator'' of the annual average convective flux or (Q_N − OLR) curve. When (Q_N − OLR) is negative, the deep ocean is giving up heat to the atmosphere and T_d declines. The opposite occurs when (Q_N − OLR) is positive.

We summarize these effects as follows. Changes in the seasonality in radiative forcing caused by the precession of the equinoxes lead to changes in convective fluxes in polar regions. The mixed layer–atmosphere respond quickly to a convective flux from the deep ocean, by heating up and thus slowing down convection (which depends on T_m − T_d in this model), and ultimately sending flux anomalies to outer space. The efficient radiation to space limits the annual average heat accumulation (or rectification) in the mixed layer–atmosphere so that precessional effects in this region are small compared to obliquity effects. On the other hand, the deep ocean, with its increased sensitivity to surface conditions at the coldest time of the year, and its long-term memory, integrates the sequence of ''precessionally forced'' convective ''anomalies'' leading to significant temperature changes in the 20 kyr band.

These features of the simple three-layer model also exist in the WS model. Figure 14 shows a high-resolution time series of global ocean temperature, (Q_N − OLR), and their amplitude spectra. The (Q_N − OLR) data are a complicated noisy signal that represents the previously mentioned high-frequency variability in T_{atm}. The series contains a burstiness with clear 20 kyr periodicity, also seen in the amplitude spectrum. In the WS model then, there *is* 20 kyr energy in the T_{atm} data, but it is very weak, as we might now expect.

Figure 15 shows the annual average fraction of convective cells from the WS ocean model together with the corresponding northern winter insolation. These signals have 20 kyr periodicity 180° out of phase with each other (i.e., there is more convection when the polar insolation is low and vice versa). Previously it was noted that T_{ocean} and northern winter insolation were 90° out of phase with each other in the 20 kyr band. If we take the fraction of convecting cells as a measure of the global convective flux, then we see that T_{ocean} acts as an integrator of the annual average convective flux just as it did in the simple three-layer convective model.

b. The 40 kyr energy and meridional variations in shortwave radiation

The above discussion uses a one-dimensional (1D) model to show how 20 kyr temperature variations can be significant in the ocean but negligible in the atmosphere. However, the anticorrelation between T_{ocean} and T_{atm} at obliquity frequencies could not be imitated by the 1D model: latitudinal resolution is required to explain this result. Obliquity forcing changes the latitudinal distribution of insolation with the equatorial and polar regions rising and falling out of phase with each other. The albedo distribution of the WS climate model results in global increases in net radiation at the same time that polar radiation is lowered. It seems possible then that increased convection due to lower polar radiation could cause the ocean temperature to fall coincident with increasing net shortwave radiation into the climate system. We used the complete version of the

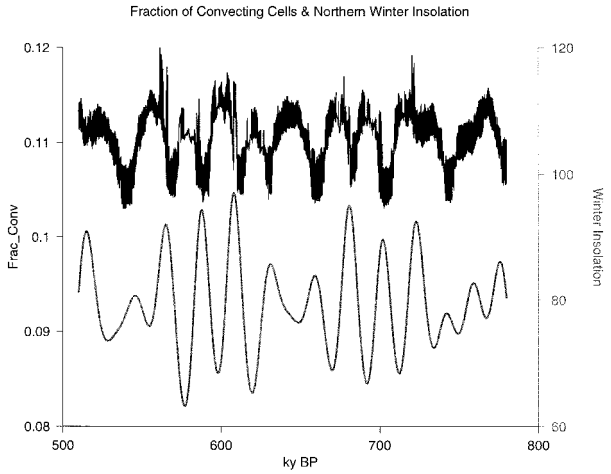

FIG. 15. The specified northern winter insolation (lower curve) and the convective activity seen in the WS model.

box climate model discussed in the appendix to test this hypothesis.

To simulate the radiation field described above, the net radiative forcing was chosen as

$$Q_N(\text{pole}) = [200.0 - Q_{12}\sin(2\pi t/40k)] + [100.0 + 5.0\cos(2\pi t/20k)] \times \cos(2\pi t/1.0) \quad (8)$$

$$Q_N(\text{eq}) = [260.0 + Q_{22}\sin(2\pi t/40k)] - [20.0 + 10.0\cos(2\pi t/20k)] \times \cos(4\pi t/1.0), \quad (9)$$

where $\delta Q_N = (Q_{22} + Q_{12})$ represents the differential obliquity forcing and the $\cos(4\pi t/1.0)$ term in the equatorial box represents the two yearly passages of the sun in this region. The constants in (8) and (9) were chosen to be consistent with the paleoradiation field analyzed from the WS model. Canonical values for Q_{12} and Q_{22} are 1.4 and 3.6, respectively.

Figure 16 shows annual averaged T_a, T_d, and Q_N from a typical model run. We see that T_a again follows Q_N, T_d has 20 kyr precessional power, and that indeed the above net radiative forcing can cause the globally averaged ocean temperature to be anticorrelated with T_a at 40 kyr periods. It was found that the response of the model depended in a complicated way on δQ_N, the convective transfer coefficient q_{conv}, and the horizontal transfer coefficients in the mixed layer and deep ocean. However, because a polar–equatorial gradient in Q_N was necessary in all cases to produce the T_a:T_d inversion effect, we conclude that the particular spatial distribution of obliquity forcing in concert with oceanic convection is responsible for the 40 kyr atmosphere–ocean temperature anticorrelation seen in the global climate model.

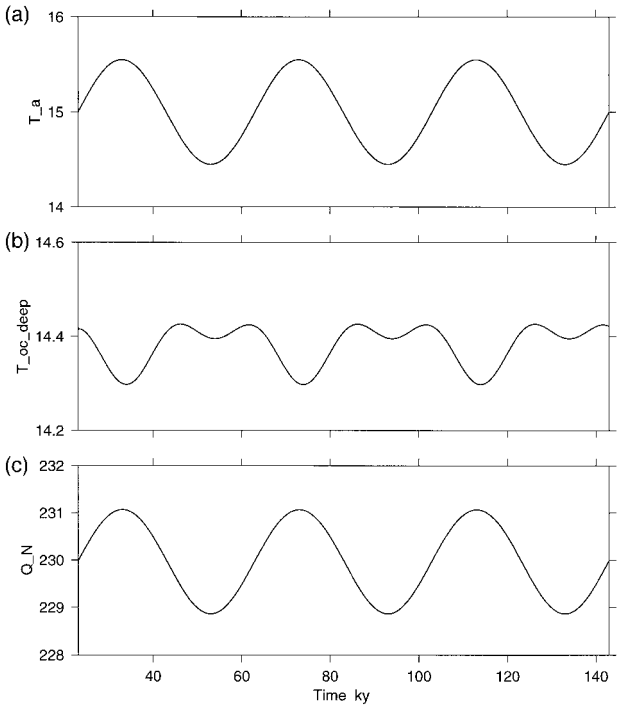

FIG. 16. Annually averaged quantities from the box climate model.

6. The ocean response in the eccentricity band

As observed in Fig. 8 the response of the global ocean in the eccentricity band is suppressed relative to T_{atm} and the forcing Q_N. The reason for this behavior relates to the nature of insolation at long periods and the equation of state of seawater.

Solar insolation averaged over the year $\overline{Q}$ increases with increasing eccentricity. To lowest order this can be expressed as

$$\overline{Q} = \frac{Q_o}{(1 - e^2)^{1/2}},$$

where e is the eccentricity and Q_o is the average insolation at zero eccentricity.

If dynamics could be neglected, these changes would have roughly the same effect on atmosphere and ocean. The slowest significant frequency in the eccentricity variation corresponds to a period of 100 kyr—far larger than oceanic diffusive timescales. However, there are at least two mechanisms in a dynamic ocean that act in the opposite direction from diffusion and tend to weaken the deep ocean response.

To lowest order a change in eccentricity affects the annually averaged insolation by the same percentage throughout the globe. However, due to the higher albedo at high latitudes, this translates to a much smaller signal in watts per square meter absorbed at high latitudes (where deep water is formed) than it does over the globe as a whole. Insofar as convection is the major driving

force for global ocean temperature changes, the deep ocean will show a smaller response to eccentricity forcing than will the atmosphere.

There is also a second, dynamic process that reduces the deep ocean response. Consider an ocean in equilibrium. Diffusion tends to heat the deep ocean, while the overturning circulation cools it by producing cold bottom water. If there were no circulation changes an eccentricity decrease would tend to cool the deep ocean by reducing the downward diffusion of heat, while an increase would have the opposite effect.

However, changes in eccentricity also affect the equator to pole density gradient and do so in such a way as to counter the change in diffusive heat flux to the deep ocean. For example, an eccentricity decrease will cool both equatorial and subpolar surface waters, but for the reasons outlined above, the cooling will be larger at the equator. In addition, the equation of state tells us that for a given (small) temperature change, the density change of warmer water will be larger than that of colder water. Thus an eccentricity decrease will result in a smaller pole to equator density gradient in surface waters and a weakening of the thermohaline circulation. The resulting dimunition in the supply of cold bottom water will allow diffusion from above to warm the deep ocean, offsetting to some degree the cooling caused by the eccentricity decrease.

Based on the above, we expect that as insolation decreases, the overturning circulation will slow down and the decrease in global ocean temperature will be correspondingly reduced. Thus Q_N, T_{ocean}, and Atl_circ should be in phase at eccentricity periods and the signal seen in T_{ocean} should be smaller than that seen in the mixed layer or the atmosphere. We have already noted from Fig. 8 that the deep ocean temperature variation at eccentricity periods is smaller than surface temperature variations. Figure 17 is a plot of the coamplitude spectra and phase for T_{ocean}–Q_N and Atl_circ–Q_N, which shows that the expected phase relations are indeed realized.

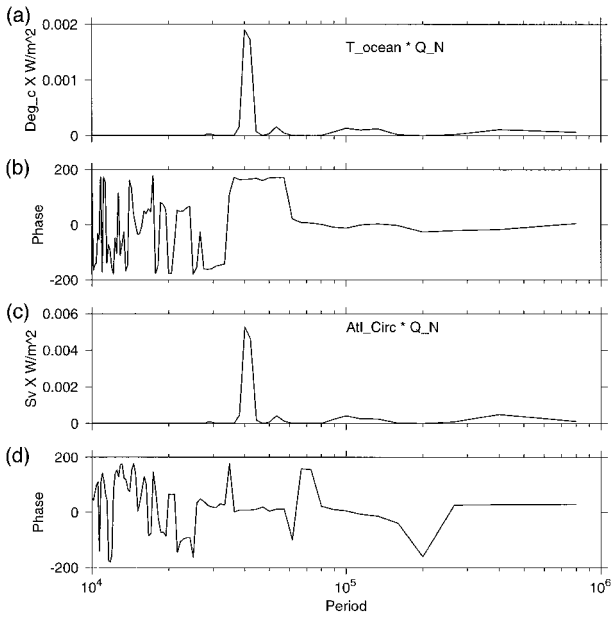

FIG. 17. Coamplitude and phase spectra of T_{ocean} and Atl_circ with Q_N.

7. Summary and conclusions

It has been known since the days of Croll and Milankovitch that insolation changes due to orbital perturbations have a distinct latitudinal and seasonal signal. The frequency and amplitude of the thermal response to these perturbations, however, is modified by the multiplicity of time constants and nonlinear processes of the climate system. For example, while hundred-thousand-year power is weak in the orbital insolation variations, it is dominant in the ice volume record of the late Pleistocene.

While the ice sheets act as an important filter on the orbital input, other components of the climate system may be of equal importance. This paper investigated the filtering of the astronomical forcing by the thermohaline circulation using a low-order coupled atmosphere–ocean climate model. We found that, indeed, this filtering was significant.

The atmosphere–mixed layer and the deep ocean respond quite differently to precessional and obliquity forcing. Changes in the longitude of perihelion (precessional changes) do not alter the annually averaged insolation received at the top of the atmosphere, tending instead to alter the strength of the seasonal cycle. Years with colder winters are compensated with warmer summers and vice versa. Thus precessional changes have an almost negligible effect on the annually averaged atmosphere–mixed layer temperature. Deep ocean temperatures, on the other hand, are sensitive not to annually averaged forcing, but to the temperature of deep-convecting water and the frequency of deep convection. Since precession affects both of these through winter temperature changes in the convecting region, there is a strong precessional signal in annually averaged deep ocean temperatures.

Obliquity forcing changes the latitudinal distribution of insolation at the top of the atmosphere, with equatorial and polar regions rising and falling out of phase with each other, without changing the global average. However, the latitudinal form of the planetary albedo leads to *global net* radiation changes that are out of phase with polar regions. This forcing, with a convecting ocean model, leads to an anticorrelation between the global ocean and atmospheric temperatures at obliquity frequencies.

One might expect the long period eccentricity changes to affect the atmosphere and deep ocean equivalently, but the mechanism that sustains deep ocean temperature

dictates otherwise. Two effects are identified. First, deep water is formed at polar latitudes, where eccentricity effects (in terms of watts per square meter absorbed) are relatively small, so the forcing felt by the deep ocean is correspondingly reduced. Second, eccentricity changes affect the pole-to-equator surface density gradient in such a way that the resulting circulation changes act to reduce the warming or cooling by diffusion from the surface. The net result is that the response of the deep ocean at eccentricity periods is suppressed relative to the atmosphere or the surface layer of the ocean.

Our simple model estimates globally averaged ocean and atmosphere temperature fluctuations of less than 0.2°. Zonally averaged values (around the entire globe) were three times this value and local values (averaged across an individual basin) two or three times larger again. Thus even local variations will not be much larger than 1° according to the present model. However, it is important to note that the results of this study are intended to demonstrate qualitative effects and quantitative estimates should not be taken very seriously. Numerous effects that might amplify temperature signals have been deliberately omitted in order to reveal qualitative tendencies in the simplest context. In particular, models that include a simple ice–albedo feedback can produce local air temperature variations of several degrees, an effect that could enhance deep convection and increase the amplitude of the deep ocean signal (e.g., Stocker et al. 1992a). Feedbacks associated with the hydrological cycle may even cause mode flips, which can result in dramatic global temperature changes (e.g., Manabe and Stouffer 1994; Nakamura and Marotzke 1994; Rahmstorf 1995). The effects of ice sheets, clouds, and changing wind fields can complicate the picture still further (e.g., Broecker 1994; Berger and Loutre 1997; Rahmstorf and England 1997).

In spite of the above caveats, it remains clear that the orbital signature can vary substantially in the vertical. In particular, seasonal variations will be largest (by far) in the atmosphere and the ocean mixed layer, but long timescale variations in the annually averaged temperature may actually be larger in the deep ocean as a result of rectification of the annual signal by deep convection. Consequently, benthic and planktonic forams in the same core might respond to quite different temperature changes, and even to different orbital parameters.

Though our results are too preliminary to be used directly in the interpretation of paleoclimatic data, it is clear that the thermohaline circulation acts as a strong filter on the Milankovitch forcing. Thus researchers should beware of drawing conclusions as to the validity of the Milankovitch theory on the basis of marine paleoclimatic records. Until we have a more complete understanding of the effects of orbital variations on the climate system, it will remain possible that two apparently contradictory records may in fact be in agreement.

Acknowledgments. Author D. Brickman was supported by the Canadian Climate Systems History and Dynamics program.

APPENDIX

An Even Simpler Climate Model

In this appendix we present a simple two-basin three-layer atmosphere–ocean climate model designed to help explain the results from the beachball model described in the main text. The idea was to devise the simplest model that can reproduce the primary results from the WS climate model. The additional simplicity helps to clarify the essential physics behind the results found in the more complicated model, and permits long runs to be done very quickly for diagnostic purposes.

This climate model is used in two different ways in the main text. To help clarify the effect of oceanic convection on climate and resolve the 20 kyr periodicity in the global ocean temperature, we need only a three-layer single-basin version. To reproduce the 40 kyr ocean–atmosphere temperature anticorrelation seen in the WS model requires at least the minimal horizontal resolution included in the two-basin formulation.

The model, shown in Fig. 9, consists of equatorial and polar basins, each with an atmosphere overlying an ocean mixed layer, and a deep ocean layer. (All vertical fluxes shown for the equatorial basin are also included in the polar basin, but they are omitted from the diagram to avoid excess clutter.) Both horizontal and vertical fluxes are modeled as a transfer coefficient (q in W m^{-2} K^{-1}) times a temperature difference so that the ratio $\tau \equiv (\rho C_P H)/q$ has units of seconds. Thus, for example,

$$F_{\rm oa} = q_{\rm oa}(T_m - T_a),$$

where $q_{\rm oa} \sim 15$ W m^{-2} K^{-1}, consistent with the Wright–Stocker model.

The flux into the deep ocean includes a convective scheme:

$$F_d = q_d(T_d - T_m),$$

where

$$q_d = \begin{cases} \dfrac{\kappa_v(\rho C_P)_o}{H_d/2} \equiv q_o & T_m > T_d \\ Q_o + q_{\rm conv} & T_m < T_d. \end{cases}$$

For $\kappa_v = 10^{-4}$ and $H_d = 4000$ m, $q_{\rm o} \sim 0.2$, and we take $q_{\rm conv} \sim 100$.

Longwave radiative transfer is as in the WS model, that is, OLR $= A + BT_a$ where $B \sim 2$ W m^{-2} K^{-1}. Interbasin exchange is modeled as

$$F_{xx} = \frac{q_{xx}}{\rho C_P(L_{\rm eq} + L_{\rm pole})/2}(\Delta T_x),$$

where $L_{\rm eq}$ and $L_{\rm pole}$ are the lengths of the equatorial and polar boxes, the subscript $x = (a, m, d)$ denotes hori-

zontal exchanges within the atmosphere, mixed layer, or deep ocean.

Using the above and the terminology from Fig. 9, the governing equations for a *single* basin of this model are

$$\frac{dT_a}{dt} = \frac{\kappa Q_n(t)}{(\rho C_P H)_a} - \frac{A + BT_a}{(\rho C_P H)_a} + \tau_{\text{ao}}^{-1}(T_m - T_a) + [F_{aa}], \tag{A1}$$

$$\frac{dT_m}{dt} = \frac{(1 - \kappa)Q_n(t)}{(\rho C_P H)_m} - \tau_{\text{oa}}^{-1}(T_m - T_a) + \tau_{md}^{-1}(T_d - T_m) + [F_{mm}], \tag{A2}$$

$$\frac{dT_d}{dt} = -\tau_{dm}^{-1}(T_d - T_m) + [F_{dd}], \tag{A3}$$

where $(\rho C_P H)_a$ denotes $(\rho_a C_{Pa} H_a)$, etc., κ is absorptivity, and atmosphere–mixed layer interactions are denoted by the subscript ao or oa.

We consider first the globally averaged model, obtained by ignoring the [bracketed] interbasin fluxes. For $H_a \sim 8$ km, $H_m \sim 100$ m, $H_d \sim 4$ km (and no convection)

$$(\rho C_P H)_a/B \sim 60d \qquad \tau_{\text{ao}} \sim 8d \qquad \tau_{\text{oa}} \sim 300d$$
$$\tau_{md} \sim 65y \qquad \tau_{dm} \sim 2500y.$$

Using these values, scale analysis of (A1)–(A2) implies a two-timescale response that decouples the deep ocean from the mixed layer and atmosphere on short timescales. Formal solution of (A1)–(A2) shows that the coupled mixed layer and atmosphere have a fast response timescale of ~7 days plus a slower spinup timescale of ~7 yr.

For paleotimescales the atmosphere and mixed layer are in quasi equilibrium (i.e., $d/dt \approx 0$) with solution

$$T_a = \frac{\kappa Q_N - A}{B} \qquad T_m = \frac{(1 - \kappa)Q_N}{q_{\text{ao}}} + T_a.$$

Letting $Q_n(t) = Q_o + Q(t)$ where $Q_o \sim 231$ and $Q(t) \sim \pm 0.25$ yields $T_a \sim 15.5 \pm 0.1°$, consistent with the result shown in Fig. 7.

Note that with no convection the equations are linear. This means that a *time mean* preserves the structure of the equations (just substitute $\overline{T}$ for T), but if the convective scheme is on, the nonlinear convective flux is such that

$$\overline{\tau_{dm}(T_d - T_m)} \neq \tau_{dm}(\overline{T_d} - \overline{T_m}).$$

Clearly, convection can serve as a mechanism for rectification of seasonal cycle forcing.

For the global model, the paleo net radiative forcing was modeled to be similar to the paleo-forcing for the beachball model, that is, as an annual-mean term that changes on a 40 kyr timescale and an amplitude modulated seasonal cycle term representing a precessional 20 kyr effect with zero annual mean:

$$Q_N(t) = \overline{Q}[1 + (1/200)\sin(2\pi t/40k)] - Q_{\text{prec}}[1 + (1/2)\sin(2\pi t/20k)]\cos(2\pi t/1.0),$$

where $\overline{Q} = 230$ and $Q_{\text{prec}} = 100$.

For the complete model the net radiative forcing was chosen as

$$Q_N(\text{pole}) = [200.0 - Q_{12}\sin(2\pi t/40k)] + [100.0 + 5.0\cos(2\pi t/20k)] \times \cos(2\pi t/1.0) \tag{A4}$$

$$Q_N(\text{eq}) = [260.0 + Q_{22}\sin(2\pi t/40k)] - [20.0 + 10.0\cos(2\pi t/20k)] \times \cos(4\pi t/1.0), \tag{A5}$$

where $\delta Q_N = (Q_{22} + Q_{12})$ represents the differential obliquity forcing and the $\cos(4\pi t/1.0)$ term in the equatorial box represents the two yearly passages of the sun in this region. The length scales L_{eq} and L_{pole} were chosen as $\pi R_E/2$, where R_E is the radius of the earth, so that an area-weighted average of (A4) and (A5) yields a $\overline{Q_N}$ equal to that of the global model. The constants in (A4) and (A5) were chosen to be consistent with the paleoradiation field analyzed from the full WS model. Canonical values for Q_{12} and Q_{22} are 1.4 and 3.6, respectively.

REFERENCES

Berger, A., and M.-F. Loutre, 1997: Paleoclimate sensitivity to CO_2 and insolation. *Ambio,* **26,** 32–37.

Broecker, W., 1994: Massive iceberg discharges as triggers for global climate change. *Nature,* **372,** 421–424.

Crutcher, H. L., and J. M. Meserve, 1970: Selected level heights, dew points, and temperatures for the Northern Hemisphere. Rep. Nav Air 50-1C-52 (revised), 8 pp. [Available from U.S. Government Printing Office, Washington, DC 20402.]

Hays, J. D., J. Imbrie, and N. J. Shackleton, 1976: Variations in the Earth's orbit: Pacemaker of the ice ages. *Science,* **194,** 1121–1132.

Herbert, T. D., and A. G. Fischer, 1986: Milankovitch climatic origin of mid-Cretaceous black shale rhythms in central Italy. *Nature,* **321,** 739–743.

Hyde, W. T., and W. R. Peltier, 1987: Sensitivity experiments with a model of the ice age cycle: The response to Milankovitch forcing. *J. Atmos. Sci.,* **44,** 1351–1374.

——, T. J. Crowley, K.-Y. Kim, and G. R. North, 1989: Comparison of GCM and energy balance model simulations of seasonal temperature changes over the past 18 000 years. *J. Climate,* **2,** 864–887.

Imbrie, J., 1984: The orbital theory of Pleistocene climate: Support from a revised chronology of the marine δO_{18} record. *Milankovitch and Climate,* A. Berger et al., Eds., D. Reidel, 269–307.

Levitus, S., 1993: Climatological atlas of the World Ocean. *Nature,* **364,** 215–218.

Manabe, S., and R. Stouffer, 1994: Multiple-century response of a coupled ocean–atmosphere model to an increase of atmospheric carbon dioxide. *J. Climate,* **7,** 5–23.

Nakamura, M., P. Stone, and J. Marotzke, 1994: Destabilzation of the thermohaline circulation by atmospheric eddy transports. *J. Climate,* **7,** 1870–1882.

North, G. R., 1975: Theory of energy balance climate models. *J. Atmos. Sci.,* **32,** 2033–2043.

Olsen, P. E., 1986: A 40-million-year lake record of early Mesozoic orbital climatic forcing. *Science,* **234,** 842–848.

Pisias, N., L. A. Mayer, T. Janecek, A. Palmer-Julson, and T. van

Andel, Eds., 1995: Paleooceanography of the eastern equatioral pacific during the neogene: Synthesis of leg 138 drilling results. *Proc. ODP Sci. Results,* **138,** 5–21.

Rahmstorf, S., 1995: Bifurfactions of the Atlantic thermohaline circulation in response to changes in the hydrological cycle. *Nature,* **378,** 145–149.

——, and M. England, 1997: Influence of Southern Hemisphere winds on North Atlantic deep water flow. *J. Phys. Oceanogr.,* **27,** 2040–2054.

Sakai, K., and W. Peltier, 1995: A simple model of the atlantic thermohaline circulation: Internal and forced variability with paleoclimatological implications. *J. Geophys. Res.,* **100** (C7), 13 455–13 479.

Saltzman, B., and A. Sutera, 1984: A model of the internal feedback system involved in late quaternary climate variations. *J. Atmos. Sci.,* **41,** 736–745.

Short, D. A., J. G. Mengel, T. J. Crowley, W. T. Hyde, and G. R. North, 1991: Filtering of Milankovitch cycles by Earth's geography. *Quat. Res.,* **35,** 157–173.

Stocker, T. F., D. G. Wright, and W. Broecker, 1992a: The influence of high latitude surface forcing on the global thermohaline circulation. *Paleoceanography,* **7,** 529–541.

——, ——, and L. A. Mysak, 1992b: A zonally averaged, coupled ocean–atmosphere model for paleoclimate studies. *J. Climate,* **5,** 773–797.

Tarasoff, L., and W. R. Peltier, 1997: Terminating the 100 kyr ice-age cycle. *J. Geophys. Res.,* **102** (D18), 21 665–21 693.

Wright, D. G., and T. F. Stocker, 1991: A zonally averaged ocean model for the thermohaline circulation. Part I: Model development and flow dynamics. *J. Phys. Oceanogr.,* **21,** 1713–1724.

Yip, K.-J., and T. J. Crowley, 1994: Selected circulation statistics and sensitivity experiments for the GENESIS GCM. Texas Center for Climate Studies Tech. Rep. 1, 29 pp. [Available from Department of Oceanography, Texas A&M University, College Station, TX 77843-3146.]